Journal of Petroleum Science and Engineering 208 (2022) 109365

Contents lists available at ScienceDirect

Journal of Petroleum Science and Engineering

journal homepage: www.elsevier.com/locate/petrol

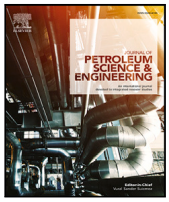

An integrated rock-mechanics tests and numerical modelling of chalk rocks: An improved integrated workflow for borehole safety

M.K. Medetbekova [a], M.R. Hajiabadi [a,*], A. Brovelli [b], H.F. Christensen [c,d], H.M. Nick [a]

[a] Danish Hydrocarbon Research and Technology Centre, Copenhagen, Denmark
[b] ISAMGEO Italia, Angera, Italy
[c] GEO, Copenhagen, Denmark
[d] Rambøll, Copenhagen, Denmark

ARTICLE INFO

Keywords:
Radial jet drilling
Austin chalk
Wellbore stability
Strain localization

ABSTRACT

Fluid withdrawal and pore pressure reduction change the effective stresses around a borehole and cause borehole instability associated with progressive localization of the damaged zone as well as potential fines production. Experimentally, chalk exhibits a complex geomechanics behaviour (pore collapse, shear failure, time/rate dependency) and modelling the behaviour of the borehole under in-situ and operational conditions requires the constitutive model to be capable of capturing the observations. This study presents a workflow that integrates rock mechanics testing on cylindrical specimens as well as specimen with a single lateral hole (SLH) and a finite element code, developed for chalk. The code incorporates post-peak softening as well as the rate dependency of the pore collapse stress in order to accurately predict the wellbore stability under in-situ stress conditions. The tested SLH specimen was CT imaged before and after testing for identifying the damaged zone and its extension. Backward numerical simulations of the SLH test data improved the accuracy of the estimated rock mechanics properties (post-peak failure and dilatancy) compared to the properties estimated by back analyses of standard triaxial tests with a single element simulator. The workflow is applied to predict the stability of a small lateral borehole (2 cm) created with Radial Jet Drilling technique with two different geometries: one with circular geometry created by a rotating nozzle; another with a circular hole with wing shaped cracks likely to develop when a static nozzle is used. Results of the wellbore stability analyses applying the chalk properties from the back analyses highlighted the importance of using experimentally verified post-peak failure and dilatancy parameters, together with a modelling tool capable of simulating shear strain localization incorporating the Cosserat approach.

1. Introduction

A detailed wellbore stability analysis is becoming increasingly important in order to construct cost-effective open-hole completions, especially for drilling methods, such as deviated, extended reach and horizontal wells (Martins et al., 1999; Christensen et al., 2004; Tan et al., 2004), and conventional and high-pressure jet drilled multi-laterals (Kamel, 2017; Reinsch et al., 2018a; Liao et al., 2020; Huang and Huang, 2019; Reinsch et al., 2018b; Medetbekova et al., 2020a). Effective stress changes around boreholes due to drilling and hydrocarbon extraction operations are responsible for instability and sanding/fines production (Radwan and Sen, 2021). During drilling, the designed mud pressure must be not only high enough to avoid the shear failure because of stress concentrations around the wellbore, but also low enough to prevent the tensile-fracturing of the formation (Zobak, 2010; Kassem et al., 2021). During production, a high drawdown pressure and depletion of the reservoir increases the sanding/fines production potential, caused by progressive development of plastic strain around the borehole. In order to design a safe operation of the well during drilling and production, a competent failure criterion and a constitutive model capable of capturing the mechanical behaviour of rock observed from experiments are required (McLean and Addis, 1990).

The chalk formations in many North Sea oil fields are high porosity chalk which are mechanically weak due to little or absence of cementation (Andersen, 1995). Based on laboratory testing, chalk shows a complex mechanical behaviour. The yield mechanisms such as shear failure, pore collapse and tensile failure are the main deformation mechanisms describing the behaviour of many rock formations. Experimentally, the shear failure occurs at a relatively low mean stress, but at high deviatoric stresses, in which solid rock grains rotate and/or

* Corresponding author.
E-mail address: mreza@dtu.dk (M.R. Hajiabadi).

https://doi.org/10.1016/j.petrol.2021.109365
Received 9 April 2021; Received in revised form 29 July 2021; Accepted 8 August 2021
Available online 14 August 2021

slide past each other on internal surfaces. Another failure mechanism is the pore collapse (compaction), occurring at high mean stress and low deviatoric stresses, associated with an increase in compressibility due to irreversible pore volume reduction. The material can also fail in tension, where rock grains are pulled apart from each other when a stress component becomes tensile (Hickman, 2004). Similar to other rock types as unconsolidated sandstones (de Waal, 1986), diatomite and calcium carbonate (Hamilton and Shafer, 1991), chalk also shows visco-plastic deformation (creep), which is a term used to describe the rate dependency of the strength (Smits et al., 1986; Monjoie et al., 1990; Andersen et al.; Andersen, 1995). Due to creep, chalk shows continued deformation under constant stress which is accompanied with a breakdown of its structure. During the last few decades, various constitutive models have been developed for chalk. Hickman (2004) provided a good review of the proposed constitutive models. Almost all the existing models have separate yield surfaces for the shearing and pore collapse, while some also include the tensile failure (Collin et al., 2002; De Gennaro et al., 2003; Homand and Shao, 2000; Plischke, 1994; Zaman et al., 1995). A few models use one enclosed yield surface for the whole mechanism (Papamichos et al., 1997; Kristiansen and Plischke, 2010). Including a pore collapse yield surface is important for the compaction analysis, while the shear failure part of the yield surface is essential for the borehole stability analysis. Among the proposed models, most ones include only strain hardening for the shear failure, which is useful for the pre-failure behaviour. To simulate the post-failure behaviour, a strain softening must be incorporated in order to capture the progressive damage associated with the reduction in the material strength.

Another complexity with chalk behaviour is that it undergoes time-dependent deformation called creep, characterized by a continuous decrease in void space as time passes, while the effective stresses remain constant (Hickman, 2004). Various rate/time dependent models have been proposed in the past, in order to simulate the creep behaviour of soft materials. Among these, empirical and rheological models (de Waal and Smits, 1988; Pruiksma et al., 2015; Bingham, 1916) are limited to uniaxial conditions. General time dependent models (De Gennaro et al., 2003; Datcheva et al., 2001; Hickman and Gutierrez, 2008; Gutierrez and Hickman, 2011; Cassiani et al., 2017; Kristiansen and Plischke, 2010; Hajiabadi and Nick, 2020; Hajiabadi et al., 2020) are adapted for implementation in the 2D/3D finite element frameworks. Since these models are not restricted to specific boundary conditions, all possible stress paths can be simulated.

Experimental and deterministic approaches are two main approaches to investigate wellbore stability (McLellan, 1996). Experimental models are based on the hollow cylinder test has been utilized as an efficient means of understanding the initiation and evolution of breakouts due to applied stresses employing the Computed Tomography (CT) scanning, as well as quantifying the production of fines from the plastified zones around the borehole as a function of fluid flow rate (Tronvoll et al., 1997; Papamichos et al., 2001; Cuss et al., 2003; Santos and Ferreira, 2015; Lv et al., 2019). Deterministic approaches including analytical solutions and numerical methods are widely used for estimating the breakout zone by considering plasticity and damage mechanic (Veeken et al., 1989; Zhang et al., 2020; Cui et al., 2020; Gao and Gray, 2020; Li et al., 2021; Abdelghany et al., 2021). Stresses induced by fluid flow into boreholes and sand production are also considered in some studies (Risnes et al., 1982; Paslay et al., 1963). Meng et al. (2019b) have studied dynamic stress distribution around the hole with considering the coupled deformation–diffusion effect. Wellbore stability is also investigated in naturally fractured formations (Meng et al., 2019a).

To date, an accurate estimate of the extent of the damaged zone associated with shear breakout by means of a model with strain softening remains challenging and only a few papers present a model validated against test data. Lv et al. (2019) proposed an analytical solution around a borehole within an elasto-softening-plastic concept; however, the solution is only applicable for a limited stress path without pore collapse incorporated into the solution. A few works take into account softening and localization in relation to borehole stability but without considering rate dependency and viscous effect in constitutive model (Papanastasiou, 2000; Papanastasiou and Vardoulakis, 1992; Papamichos, 2010).

The present work aims to demonstrate how the prediction of the wellbore stability analysis in chalk can be improved through the integration of rock-mechanics test data as well as numerical modelling data. The work also demonstrates the significance of using an experimentally validated modelling tool capable of predicting post-peak softening as well as rate dependency of pore collapse stresses under field conditions. A workflow developed for stability analyses and for obtaining the required rock properties is based on five main parts: 1. the basic rock mechanics testing for estimating the rock properties; 2. a rock mechanics testing method, called the single lateral hole (SLH), to study the wellbore stability under various stress paths, creep and flow conditions; 3. utilizing CT imaging for identifying the damaged zone and its extension, and 4. backward numerical simulations of the SLH test data to improve the estimated rock mechanics properties and 5. forward numerical simulations utilizing the estimated properties to predict the stability of open-hole in chalk under reservoir in-situ stresses and operational conditions.

2. Methodology of the wellbore stability analysis

The workflow for the wellbore stability analysis builds upon a methodology illustrated in Fig. 1, which integrates standard rock mechanics testing, single hole lateral testing, finite element modelling using single element approach as well as 2D/3D modelling for predicting material parameters, and CT scanning. The triaxial tests were carried out on standard cylindrical specimens and the test program was designed in order to establish a model that captures the pore collapse and the shear failure yield surface in the $p' - q$ diagram. The single lateral hole test was designed in order to study the wellbore stability under various loading, creep and flow conditions. The CT imaging was used after each loading step of the SLH specimen for a preset stress in order to evaluate the extent of the damaged zone around the hole. Numerical backward analyses were carried out by the single element (SE) and 2D/3D modelling. Modelling of the triaxial test using the SE simulator enables prediction of the first estimations of the rock mechanical properties, whereas modelling by means of the 2D/3D mesh improves the accuracy of the predicted parameters, especially for the parameters representing the post peak failure and dilatancy. Forward modelling of the openhole stability with considering in-situ stress condition, drawdown and depletion scheme were carried out with a 2D mesh utilizing the estimated properties from the back analyses of the SLH test. In this paper, numerical analyses are performed using the ISAMGEO simulator, employing the chalk model (Cassiani et al., 2017), which is adopted to take into account the post-peak shear softening and the rate dependency of pore collapse deformation. The model benefits from two independent yield surfaces for the shear failure and the pore collapse yielding surface (Medetbekova et al., 2020c). The shear failure is given by Mohr–Coulomb criterion with hardening and softening effects. The yield surface for the pore collapse is given by a shifted elliptical cap, similar as for Modified Cam–Clay model (Roscoe and Burland, 1968). While the shear failure is assumed rate-independent, the pore collapse yield surface can shrink and expand not only by softening or hardening affect, but also by softening/hardening volumetric plastic strain rate effects. The constitutive model is described in Appendix A.

2.1. Standard rock mechanics testing

Conventional triaxial compression tests were performed in accordance with standard ISRM test procedures on cylindrical core specimens (ISRM, 1983). Three triaxial compression test were performed

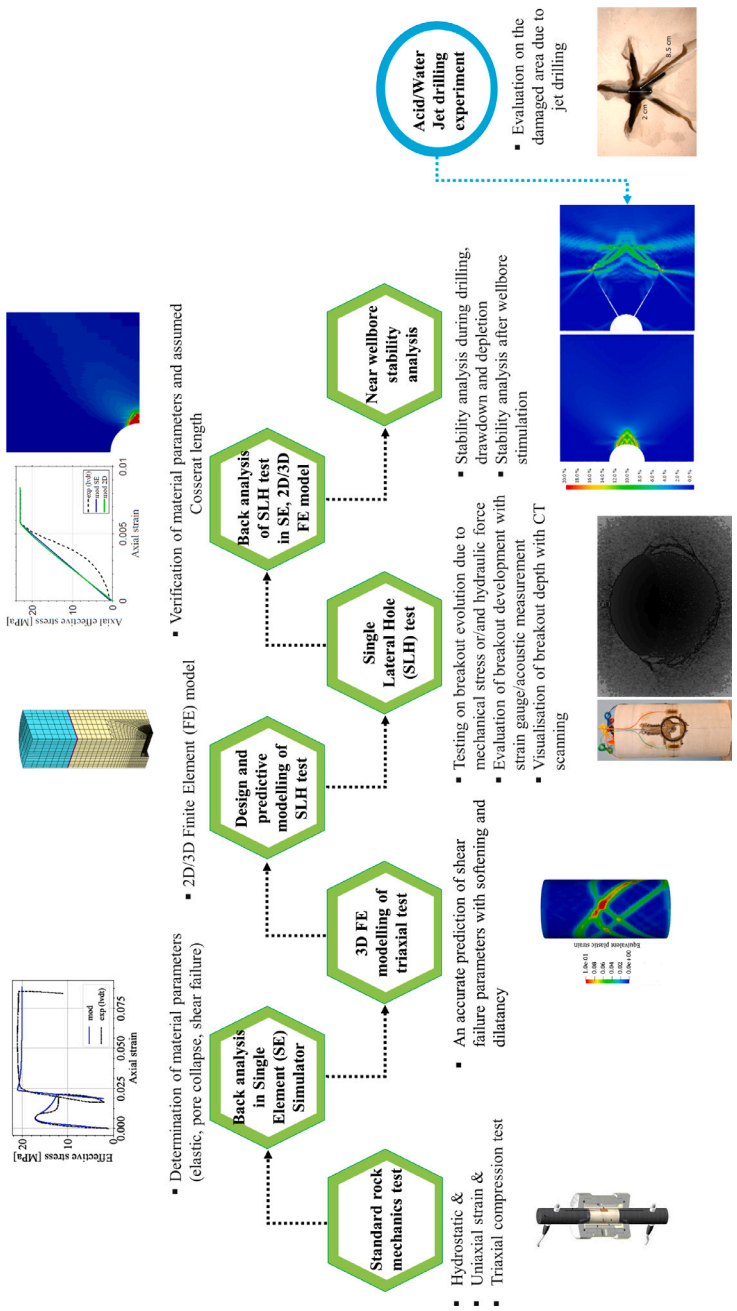

Fig. 1. Workflow for the wellbore stability analysis.

to establish the shear failure yield surface as the specimen was loaded under an axial compression at two consecutive confining stresses. From the hydrostatic compression test the pore collapse behaviour was determined by pressurizing the sample equally in all directions. One uniaxial compression test is also required to allow the pore collapse yield surface calibration. It involves compressing the sample between two rigid plate while the lateral displacement retained to zero by correcting the volume changes. A uniaxial compression test followed by a creep phase allows to obtain the rate dependent yielding cap. It should be emphasized that we only performed a hydrostatic compression test here to determine pore collapse. Other parameters for the yielding cap (e.g. creep parameter) are extracted from uniaxial compression test followed by a creep phase estimated for Gorm chalk field (Medetbekova et al., 2020c).

2.2. Back analysis using single element simulator

The conventional triaxial compression tests were back analysed by a single element simulator. Although it would be possible to do this by performing a single calculating the stress–strain integration, single element simulator benefits from using a single element with boundary conditions of the triaxial setup in the finite element code ISAMGEO.

Due to the homogeneous stress and strain condition within the specimen, the single element approach fails to model the localization of deformation along the discrete shear plane. It smears the strains over the whole element representing the rock specimen associated with the average strain in the specimen. Thus the shear failure parameters with softening and dilatancy can vary from the refined finite grid model where strain localization is a product of the simulation (Christensen et al., 2004). However, this tool is quick for calibration of the basic

material properties such as elastic, pore collapse strength and shear failure parameters derived from the stress–strain curve.

2.3. Modelling of triaxial compression test in 3D

Since the single element approach gives only approximations for material parameters, an accurate prediction of the shear failure parameters with dilatancy and softening behaviour requires running additional 3D modelling of the triaxial compression test. The strong dilatancy and softening behaviour observed in the experiments is not an intrinsic behaviour of the material, but rather the effect of the bifurcation of the deformation pattern. Typical examples of such inhomogeneous deformation are the barrelling, buckling and shear band formation. Heterogeneity of the material properties, boundary conditions such as end constraints and confinement, and also the shape/size of the specimen are the typical causes of inhomogeneous deformation (Sulem and Vardoulakis, 1991). Unless the imperfections are introduced, numerical modelling of the triaxial test causes barrelling of the specimen. The imperfections can be introduced as the applied load or heterogeneity of properties. In this study, the latter approach was utilized with randomly (uncorrelated) assigned chalk parameters scattered over the chalk specimen sampled from a gaussian distribution. The finite element (FE) model simulated the applied displacement at the top of the piston centre. The simulation was initiated with a hydrostatic stress state of 2 MPa followed by prescribed vertical displacement at the top of the piston while the confining stress remaining at initial stress of 2 MPa.

Material models exhibiting softening behaviour and stiffness degradation often lead to severe convergence difficulties in implicit analysis programs. The model uses Cosserat continuum to overcome these convergence difficulties (Khoei, 2010; Vardoulakis, 2018). Cosserat continuum with incorporating an intrinsic material length scale into the conventional continuum mechanics approaches departs from the local theories to account for size effects in the mechanical behaviour.

The modelled specimen had a height of 108 mm and a diameter of 54 mm. The model consists of 38016 20-node quadratic brick elements (Fig. 2). These elements were assigned to a set of 10 different material types, taken from the numerical back analysis of the standard test using the single element approach. Above and below the chalk specimen, interface elements with 2 mm thickness (modelling the steel filter plate) were used which had a Young's modulus of 7 GPa, while the pistons had a Young's modulus of 210 GPa. Due to the stiffness contrast steel-chalk, the stress distribution in the interface is not uniform (a similar case is well known in foundation engineering: a loaded stiff plate on a soft ground). The finite element subdivision of the piston must be sufficiently fine to model the associated stress redistribution in the piston. The interface elements were introduced in order to reduce the end plate friction effect and also the stiffness contrast between the piston and chalk.

2.4. A predictive model for the single hole test

As it was required to dismount the test set-up for CT scanning, it was necessary to run a predictive model for the SLH test to determine the stress state at which the breakouts start developing around the horizontal hole. The specimen was loaded with radial effective stress to axial effective stress ratio (K) of 0.4. This stress ratio is chosen close to the uniaxial compression condition when the pore collapse deformation achieved. Thus modelling of the SLH test by means of a 2D simulation under plane strain condition can represent the results of the 3D simulation around the circular hole. It should be mentioned that a 3D simulation with the given dimensions was first performed to assure the chosen width of the pillar is sufficient to prevent boundary effects and avoid global failure due to shear failure at the pillar. Then 2D simulations were preferred to reduce computational costs utilizing a fine mesh.

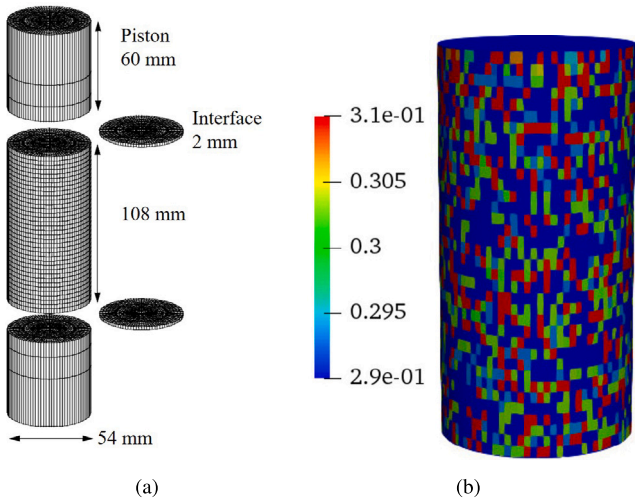

Fig. 2. Triaxial Compression test: (a) 3D triaxial test model (b) Illustration of a randomly generated porosity field. 10 different material types represented by a porosity value for each type were assigned.

Fig. 3 shows 2D and 3D meshes for the SLH test. The specimen had the following dimensions: 98.6 mm diameter, 197.6 mm length, and 20.44 mm hole diameter. In the 3D model, the pillar width was 19 mm. The 2D geometry was modelled with 3386 higher order finite elements, while the 3D geometry comprised of 25749 elements. Due to symmetry, the 2D model considered 1/4 of the full geometry, while the 3D model considered 1/8. As in the triaxial compression test model, above and below the sample, interface elements (with 1 mm thickness) were also used for modelling the SLH test. At a determined level of stress, testing continued with subsequent constant stress (creep) phase.

2.5. Rock mechanics test with horizontal hole

The SLH test was carried out on a test specimen with a diameter of 98.6 mm and a height of 198 mm (Fig. 4). A 'horizontal wellbore' hole was drilled laterally at the centre of the specimen, to a depth corresponding to about 2 cm from the outside perimeter of the specimen. Afterwards, a slightly bigger hole (plug hole) was drilled to a depth of about 2.3 cm. The reason for this was that the 'horizontal wellbore' had to be sealed inside the test specimen, otherwise the outside rubber membrane supplying the confining pressure would enter the hole when the specimen was being loaded. Then the borehole was sealed by a plug of similar chalk material. The plug was carefully shaped to fit the SLH test specimen. A tiny hole was made at the centre of the plug and a steel tubing connecting to the inner wellbore was installed through the tiny hole. After installation of the plug, the tubing was sealed with epoxy rubber to prevent leakage. The rim of the plug was also sealed with epoxy rubber, to prevent the membrane entering the borehole due to confining pressure and to prevent the plug to fail in tension due to axial loading. The strain gauges were installed, and the wires and tubing were aligned and fixed before the specimen was enclosed by the inner rubber membrane. Finally the specimen was installed in the Hoek cell and mounted in the load frame, and the Linear Voltage Displacement Transducer's (LVDT) were aligned. In total 5 axial strain gauges and 2 LVDT's were used for measuring the axial deformation, while 3 radial strain gauges were installed to measure the radial deformation.

Using the material properties derived from the numerical back analyses of standard triaxial tests with the single element simulator and 3D triaxial compressive test modelling, it is possible to run a predictive model in order to identify at which stress level the breakouts are expected avoiding the global failure of the specimen. At the end of the test, the specimen was unloaded and CT scanned for the visualization of

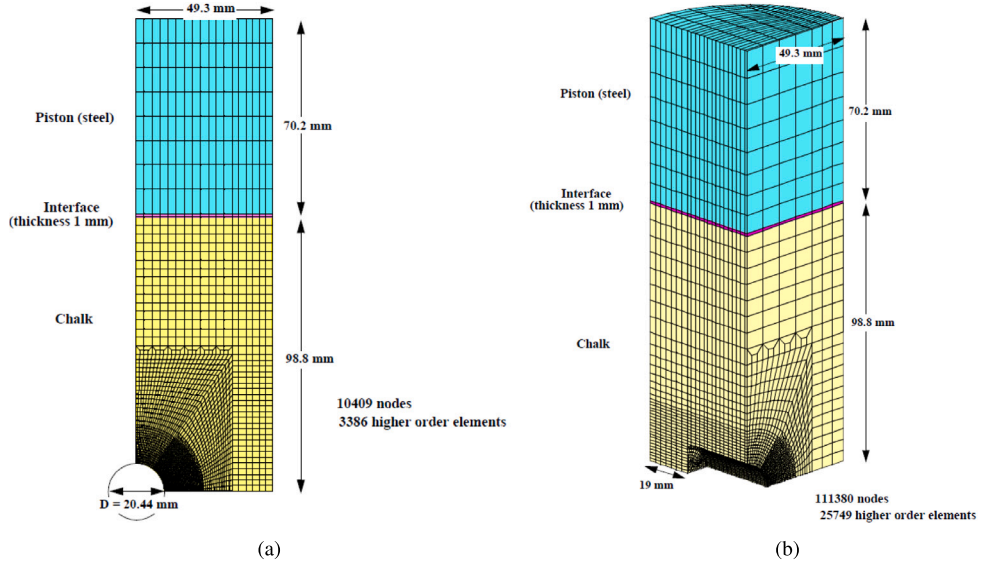

Fig. 3. (a) The 2D and (b) 3D schematics of a specimen with a single lateral hole (SLH) meshed in the finite element model.

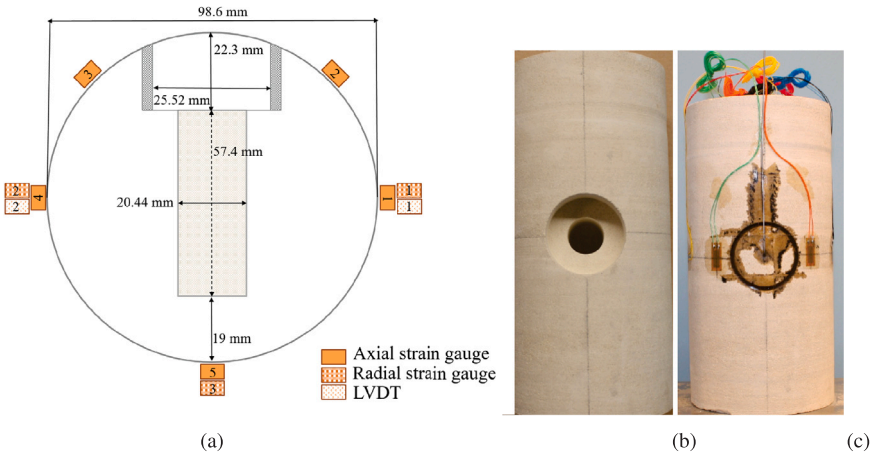

Fig. 4. Design of the single lateral hole test: (a) Top view schematic of the specimen and positioning of the axial/radial strain gauges and LVDT; (b) Austin chalk specimen (length 200 mm, diameter 100 mm) drilled laterally with a horizontal hole (length 57.4 mm, diameter 20.44 mm) and plug hole (length 22.3 mm, diameter 25.52 mm); (c) Illustration of the specimen sealed with the plug hole and glued with the strain gauges.

break-out development and verification of the extent predicted with the model. Evaluation of the breakout development with increasing applied effective stresses was made by monitoring of the strain development from strain gauges.

2.6. Modelling of the single hole test

As mentioned earlier the 3D triaxial compression test modelling provides the first estimations of the softening and dilatancy post-peak strength and stiffness parameters. Indeed, those parameters are better approximations than those predicted from the single element approach. However, further unknown is whether the shear band thickness modelled with 3D modelling is truly representing the shear zone development observed in the triaxial compression testing. Backward modelling of the SLH test enables us to verify the softening and dilatancy parameters to reduce uncertainties. Moreover, the assumed Cosserat length that was used in the triaxial test can also be verified with the back analysis of the SLH test.

2.7. Near wellbore stability analysis

Jet drilling experiments carried out by Medetbekova et al. (2020a) on outcrop Austin (US) and Welton outcrop (UK) chalks suggest that depending on the nozzle type, different borehole geometries can be created. Using the rotating nozzle with water, a circular borehole geometry with a diameter of about 2–3 cm can be created, whereas with the static nozzle with acid aided fluid, a circular geometry with wings with a diameter of 2 cm and wing cracks extension of 2–3 cm can be obtained. Moreover, analysis of the rock mechanics properties of chalk after jet drilling with acid aided fluid suggested a local damage of the chalk, where strength and stiffness properties are significantly reduced and porosity near the borehole is increased (Medetbekova et al., 2020b). In this study, the stability of the lateral borehole was investigated with a two-dimensional mesh and for two different geometries illustrated in Fig. 5. It is common to use plane strain condition for main boreholes. But under special conditions, plain strain condition can be violated in some places. Especially at junctions where lateral boreholes deviate radially from the main borehole, plain strain condition is not a true assumption. However, plain strain condition is assumed here. The 2D geometry with circular hole was modelled with 2772 higher order finite elements, while the geometry with wings was modelled with 4416 higher order finite elements. The detailed view of the model shows that the borehole has a 10 mm radius and that the model with the wing has a wing depth of 30 mm and width of 2 mm. Assuming symmetry, one fourth of the cross section was modelled.

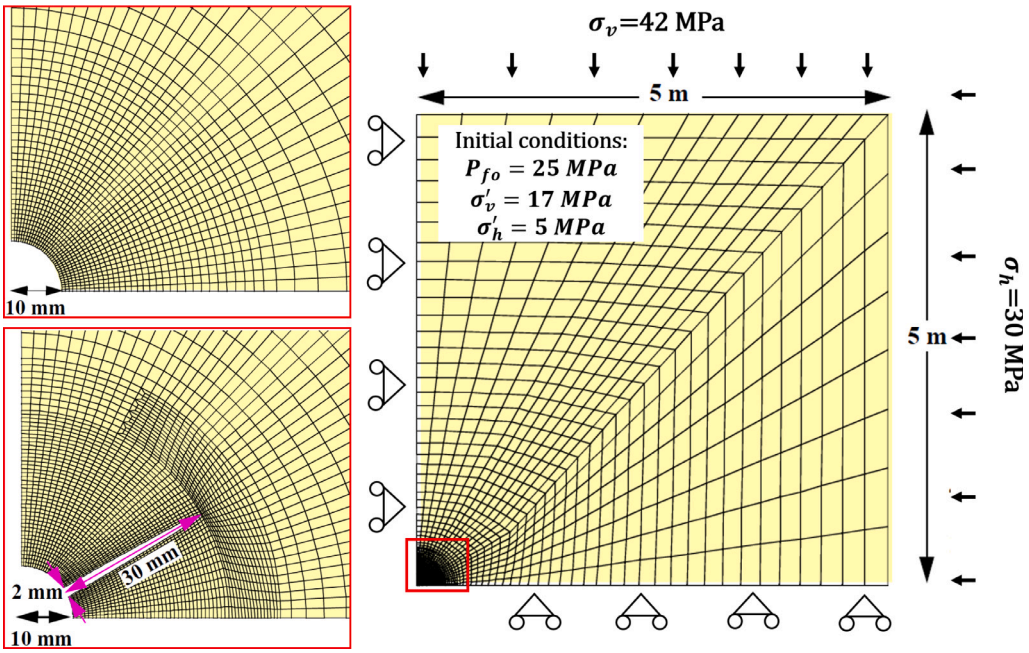

Fig. 5. Finite element mesh for the stability analysis of a horizontal openhole lateral, assuming plane strain conditions. The model has a length 5 m and a height of 5 m. A close up of the near borehole area shows that the diameter of the lateral is 10 mm. In the borehole geometry with the wing, the depth of the wing is 30 mm and the width is 2 mm. Applied initial conditions to the model: effective vertical stress of 17 MPa, effective horizontal stress of 5 MPa and reservoir fluid pressure of 25 MPa.

In the wellbore stability simulation, the following initial conditions were applied: Effective vertical stress of 17 MPa, effective (isotropic) horizontal stress of 5 MPa and initial reservoir fluid pressure of 25 MPa. The simulations were carried out in three steps:

1. During the first step, initial conditions (pore pressure, stresses) were applied, then the drilling phase of the wellbore was simulated with the effective stresses being reduced to zero for elements inside the drilled area lasting for 12 h followed by 2 days of constant stress phase. As in the Radial Jet Drilling the technique does not use drilling mud, the pressure change in the well was kept at zero.
2. In the second step, for over two days, the production phase was simulated with reduction of the wellbore pressure by 2 MPa. The pressure is kept constant at the outer boundary.
3. The third step simulated the reservoir depletion, in which the pore pressure at the outer boundary was declined by 9 MPa and the wellbore pressure by 10 MPa for over four days with subsequent creep phase of about 50 days.

2.8. Outcrop chalk material

The chalk material used in this study was from the Austin quarry in Texas, US. Austin outcrop chalk characterized as a fine-grained carbonate mud deposit, predominantly composed of well-preserved and debris of coccoliths, planktonic foraminifera and calcispheres (Cloud, 1975; Dravis, 1980). Using the carbonate-texture classification of (Dunham, 1962), the Austin chalk is categorized as wackestones to packstones, with packstone as the dominant texture. An average of 88% calcite content for the Austin outcrop specimens is identified from X-ray diffraction analysis (Corbett et al., 1987). For the triaxial tests, the specimens were end trimmed to the final length of about 7.6 cm and diameter of 3.8 cm, whereas for the SLH test length of about 200 cm and diameter of 10 cm. The porosity of the specimens for the triaxial tests was in the range of 30%–31% (estimated based on a grain density of 2.71 g/cm^3). The porosity of the specimen prepared for the SLH test was 25.4%.

3. Results

3.1. Back analysis of standard triaxial tests

In total four rock mechanics tests were carried out on intact specimens. A hydrostatic compression test on specimen 4 included loading beyond the pore collapse strength was performed. Two stage triaxial compression tests were carried out on specimens 11, 7 and 10. The specimen 11 was tested with 2 MPa and 4 MPa of confining pressure during the first and second shear phases, respectively. The specimen 7 was tested with 4 MPa confining pressure during the first shear phase and with 2 MPa confining pressure during the second shear phase. The specimen 10 was tested with constant confining stress of 6 MPa and 4 MPa, during the first and second shear phases, respectively.

The performed standard rock mechanics tests were back analysed by means of the single element simulator under the strain control condition. In the single element, modelling of the standard tests was strain controlled. With regards to the strain curves, preference was made to match the external LVDT measurement as opposed to the internal measurements obtained by the strain gauge. Compared to the local strain gauge measurement, that represents centimetre scale deformation, the LVDT displacement measurement may also include closing of micro-fractures and bedding effects. Thus, the LVDT tends to register more axial deformation than the axial strain gauges.

Table 1, first column lists parameters used for the numerical back analyses of the standard triaxial tests using the single element simulator. Since only multi-stage triaxial compression tests were designed for this study, it was attempted to match the stress–strain curves at the three phases with a single parameter set, but it was not always possible, due to the material behaviour. One of the reasons for this is that the state of the applied stress in the test was in the transition zone between the pore collapse and the shear failure. This change in stress state turned out to be sensitive to several parameters, most significantly to the angle of friction, dilatancy, cohesion, equivalent plastic strain, and the creep parameter. Therefore, the average values with variances for material parameters of the four rock mechanics tests are shown in first column of Table 1. The results of single element simulator for four rock mechanics tests are summarized in Fig. 6. According to this Figure,

Table 1
Estimated chalk mechanical properties.

Parameters[a]	Average(Variance)[b]	Specimen 11[c]	SLH test[d]
Porosity, ϕ	0.31(0.005)	0.28–0.3	0.25
Young's modulus, E [MPa]	3650(300)	3900–4300	3900
Poisson's ratio, *nu*	0.21	0.21	0.21
Angle of friction, $\varphi_{ini/peak/res}$ [°]	33(1.0)/38(1.6)/37(1.6)	33–35/38–40/37.8–39.8	34/39.5/38.8
Dilatancy, $\psi_{ini/peak/res}$ [°]	0/2.6 (2.1)/1 (1.7)	4/9/5	2/6/3
Cohesion, $c_{in=peak/res}$ [MPa]	1.6(0.4)/0.7(0.1)	1.9–2.3/0.15–0.25	3.1/0.7
Pore collapse strength, P_c [MPa]	23.7 (1.4)	23–25	26
Hardening, h_c/h_n [MPa]	1530/2600	1530/2600	1530/2600
Semi-axis ratio of ellipse, M	1.5(0.05)	1.5–1.6	1.5
A_0 [MPa]	1.6(0.1)	1.4–1.6	1.5
Creep rate coefficient, *b*	0.066(0.007)	0.05–0.065	0.05
Equivalent plastic strain at peak, e_{pl}^{peak} [%]	0.57(0.2)	0.4–0.6	0.5
Friction softening, χ	10–65	35	15
Cohesion softening, θ	8–65 (Exponential)	70(Linear)	16(Linear)
Impact of intermediate principal stress, ζ	–	0.02	0.06
Cosserat length, *l* [m]	–	5E−05	5E−05

[a]Permeability of all samples are within the range 0.3–0.6 md.
[b]Using single element simulator for Specimens 4, 7, 10, and 11.
[c]Using the 3D numerical model of triaxial compression test for the specimen 11 at constant confining stress of 2 MPa.
[d]Using the numerical model of SLH.

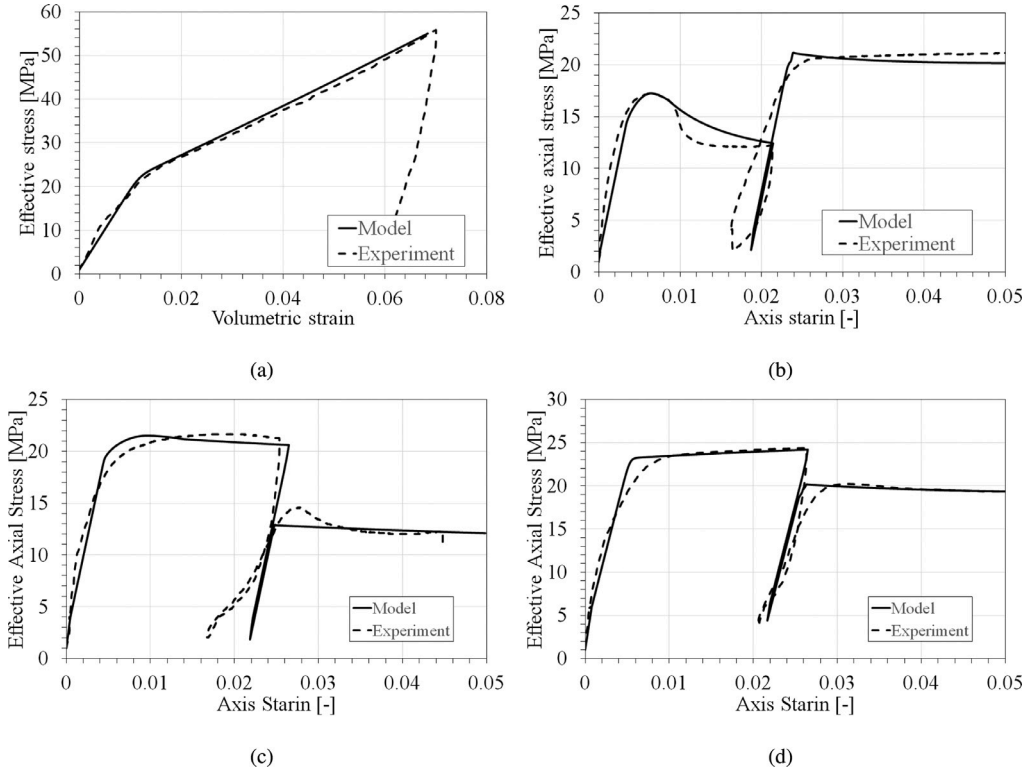

Fig. 6. Back analysis of stress–strain curves for (a) specimen 4 tested under Hydrostatic compression test and three other tests under triaxial compression test with two stages of different confining stresses including (b) specimen 11 tested at 2 & 4 MPa confining stresses, (c) specimen 7 tested at 4 & 2 MPa confining stresses and (d) specimen 10 tested at 6 & 4 MPa confining stresses.

good agreements are seen between the simulation and experimental results.

A triaxial compression test with 2 MPa confining pressure was simulated with 3D model. Fig. 7 illustrates the axial stress in the centre of the top piston versus applied axial strain. In this plot, the test results compared to the results obtained with the single element and 3D numerical modelling. In the single element model the strain development within the specimen corresponds to the average strain, thus modelling the shear strain localization is not possible. Although the peak strength is well captured with both of approaches, the post peak softening behaviour is less pronounced using 3D modelling compared to the single element approach. In 3D model, cohesion softening together with Cosserat length and intermediate principle stress are improved for the best agreements between experimental and numerical results (Table 1, second column).

3.2. SLH test

Fig. 8 presents test data obtained for SLH 1 specimen tested under triaxial compaction with fixed stress ratio of 0.4, in which the specimen was loaded to an effective axial stress of 23 MPa and a radial stress of 9.2 MPa and left to creep for more than 35 h. The time history of the effective axial and radial stresses deviate from linearity in the beginning of the test. Since the test was carried out with a fixed stress ratio,

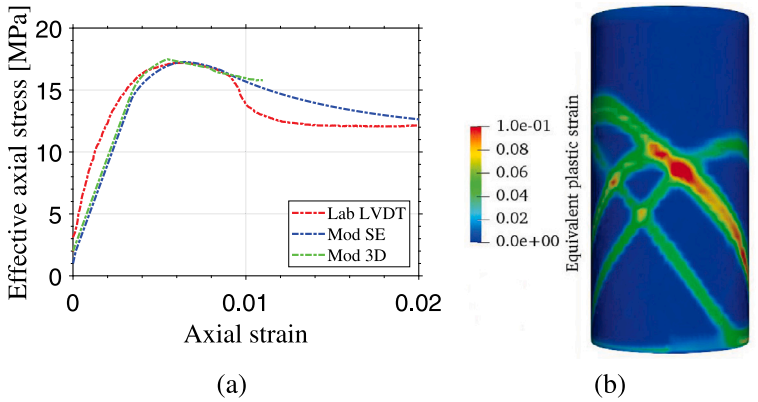

Fig. 7. Specimen 11 tested under triaxial compression at 2 MPa confining stress during first compression loading: (a) Model prediction of the axial strain with single element (mod SE) and 3D mesh (mod 3D) and measured axial strain from LVDT (Lab LVDT) plotted against effective axial stress; (b) Development of shear bands on the specimen represented by equivalent plastic strain.

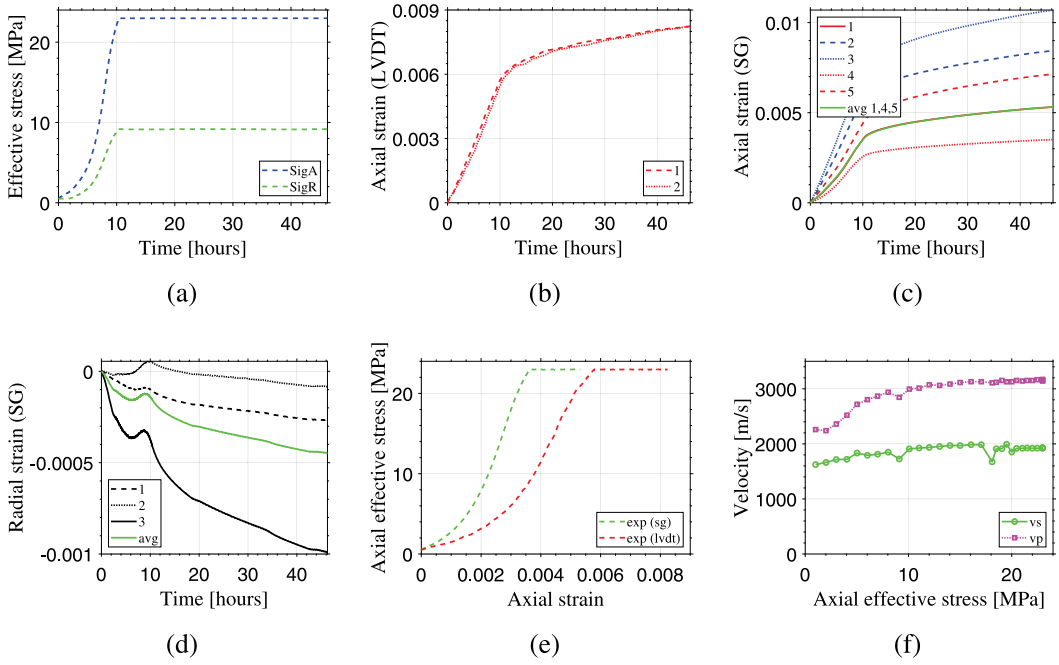

Fig. 8. Single hole testing: (a) Time history of applied effective axial (SigA) and radial stresses (SigR); (b) Time history of axial strain from LVDT measurement; (c) Time history of axial strain from strain gauge measurements; (d) Time history of radial strain from strain gauge measurements; (e) Plot of axial strain from LVDT (exp lvdt) and strain gauge (exp sg) measurements versus effective axial stress; (f) Development of the compressional (vp) and shear wave (vs) velocities with increased effective axial stress. Sudden spikes are observed in shear wave velocity approaching 10 MPa and 20 MPa may indicate grain slip and pore collapse deformation.

meaning that the load frame goes forward with strain rate of 0.1%/h and the confining pressure is then adjusted to 0.4 of the obtained axial stress. In the beginning, the confining pressure pump may be lagging a bit behind (due to the large cell volume) and it also requires some vertical deformation for the vertical stress to build up. The reason for the test not being carried out stress controlled is, because shear failure (and to some degree also pore collapse) will cause rapid increase in the strain rate, not allowing testing in a controlled way in the post-shear phase. As can be seen, the recording of two axial strains measured from LVDT have comparable values. In contrast, the measurement of axial strains from strain gauges showed the highest strain value for the strain gauges placed adjacent to the hole from both sides (2 and 3 in Fig. 4), whereas the strain gauge 5 placed at the plug showed slightly higher values compared to those placed at the centre edge (1 and 4 in Fig. 4). Similar to the axial strain gauges, the measurement of the radial strain gauges recorded the highest strain at the plug (3 in Fig. 4), compared to those placed at the mid edge (1 and 2 in Fig. 4).

The plot of the shear/compressional wave velocities versus effective axial stress shows the change in velocities in the course of increased effective axial stress. The plot shows that when the single hole specimen is subjected to an effective axial stress up to 10 MPa, both of the velocities increased gradually. Beyond this effective axial stress level, both of the velocities levels out and remained almost constant values while increasing the effective axial stress to 21 MPa and also in the subsequent creep phase. As the stress path in the single lateral hole test was carried out with an effective stress ratio of 0.4, meaning that there was an increasing confining pressure support on the specimen with increasing the effective axial stress. The initial increase of the velocities could be related to the closure of the randomly oriented microcracks within the specimen, whereas the levelling out of the velocity at a later stage could be explained with pore collapse mechanisms, that triggers grain boundary slip, grain rotation and calcite twinning, thereby leading the shear/compressional wave velocities to stabilize, as observed by Mowar et al. (1996) from testing Austin chalk in conventional triaxial compression test at high confining stress. It could be possible

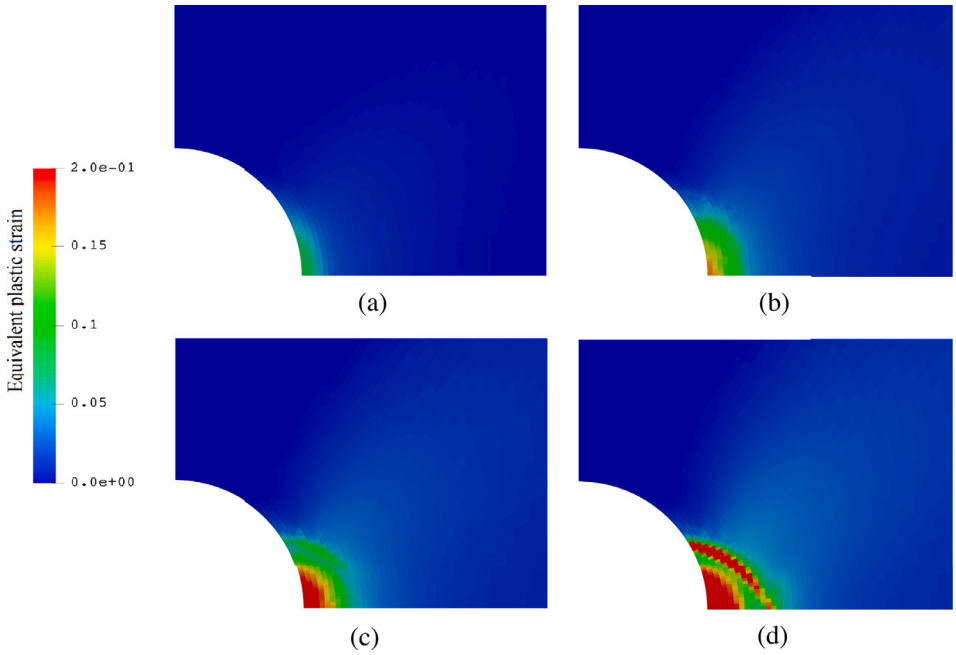

Fig. 9. Evolution of the breakout during creep phase after loading to 23 MPa axial stress within loading time 10.3 h under stress ratio of 0.4 at creep time (a) t_{cr} = 0.0; (b) t_{cr} = 7.7; (c) t_{cr} = 18.3; and (d) t_{cr} = 36.0 h.

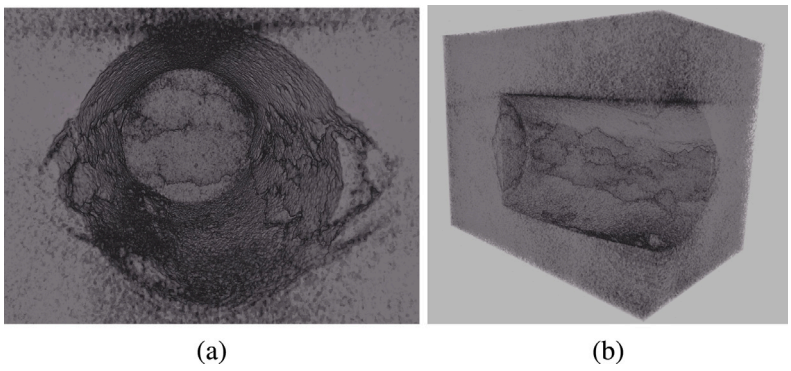

Fig. 10. (a) CT visualization of the breakouts developed at the lateral hole wall; (b) Side view of the horizontal hole wall from CT scanning showing the frictional shear breakouts developed along the length of the hole.

that these micromechanisms are active away from the hole where confining stresses are high. However around the hole, at the free surface where stresses are concentrated, shear fracture development should be initiated.

The breakout development at the lateral hole wall was inspected by CT scanning and shown in Fig. 10. For the applied effective axial stress of 23 MPa, breakouts developed forward towards the rock from the hole wall towards the applied minimum stress direction. In addition, loose grains spalling off from the crack surface can also be observed. According to (Haimson, 2007), there exists several distinct failure micromechanisms as intra- and trans-granular dilatant microcracks mainly observed in crystalline granite, intra- and inter-granular dilatant microcracks in Indiana limestone, intra-granular extensive microcracks in well cemented arcosic sandstone. (Haimson, 2007) describes that the cracks appear to be dislodged from the rock matrix in weaker limestone, such as the Austin chalk, by frictional shear between the crack walls. At a higher differential stress than 13.8 MPa, the microcracks are likely to deepen and continuously narrow as the spalled flakes become shorter, leading to dog-eared breakouts.

3.3. Back analysis results of SLH test

One of the aims of back analysis of the SLH test was verification of the softening parameters after post-peak and dilatancy angle, as well as of the assumed Cosserat length estimated from 3D modelling of the triaxial test. While common triaxial tests are enough to calibrate pre-failure behaviour, back analysis results of SLH test shows the material parameters relating to the post failure like softening parameters must be calibrated in an open hole test.

Fig. 9 illustrates the evolution of the calculated equivalent plastic strains during creep phase. As observed in this figure, significant development of breakout zone during creep phase due to continuous deformation occurs in the sample. The model performed well with regards to capturing the formation of the breakouts corresponding to the ones visualized in Fig. 10 obtained from CT scan at the end of the creep phase, where shear cracks started to deepen and increased spatially, reproducing the dog-ears as observed in the test. Fig. 11 shows the axial strains calculated at the top of the piston. Time history of the strain plot shows that the results match well with the experiment during the creep phase.

Generally, back analysis of the SLH test must use the same basic parameters for the shear failure and pore collapse, as well as for the

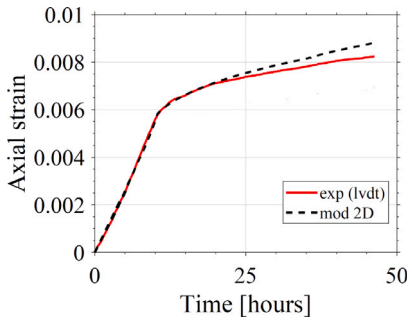

Fig. 11. Time history of axial strain measured from LVDT (exp lvdt) in SLH test modelled with 2D simulation.

elastic parameters from the single element approach, while tuning the softening, dilatancy, and Cosserat length. However, the specimen prepared for the SLH test had lower porosity (25.4%) compared to those specimens prepared for the triaxial test (30%–31%). Thus, some parameters were changed (Table 1). A sensitivity analysis given in Appendix A on break out zone to the variation in material parameters demonstrates the ability of the model to predict different scenario of the damaged zone in SLH test.

3.4. Wellbore stability analysis

For the wellbore stability analysis, the chalk properties derived from the back analysis of the SLH test were used as input into the simulator (Table 1 , last column). The fluid was considered as incompressible and the permeability of porous media was set to 0.5 md and Biot coefficient is assumed to be 1. Fig. 12 a represents the calculated equivalent plastic strain after reducing the bottom hole pressure by 12 MPa and the fluid pressure by 9 MPa at boundaries of 5 m, where the development of the shear breakouts at the borehole wall can be observed. Fig. 12b represents a continuation of the simulation under constant stress conditions over 50 days, which provided pronounced localization of the damaged zone at the borehole wall and further development of the breakouts into the chalk. Fig. 12c illustrates a stability analysis for the borehole with wing geometry with the same conditions applied as for the circular geometry. For this geometry, after the bottom hole pressure was declined by 6 MPa and fluid pressure was declined by 3.8 MPa at boundaries of 5 m, wings nearly closed and the plastic strain concentrated at the tips of the wings.

According to the simulated results, the role of the creep deformation in wellbore stability demonstrates the possibility of breakout development in open hole section in long terms. This finding can help to improve the criteria to achieve safe mud-weight window and optimize the bean up operations for open hole sections. Safe mud-weight window refers to the range of fluid density that is required in wellbore to avoid compressive and tensile failure. Bean-up operations refers to process of gradually increasing the rate or drawdown towards achieving a stabilized rate. To the best of our knowledge, the effect of creep deformation is not considered in failure criteria for the analysis and design of the safe mud-weight window and bean-up operation. Neglecting the effect of creep deformation in failure criteria in bean-up management can cause severe damage in uncased sections which is likely to happen followed by frequently and harsh shutdowns.

4. Conclusion

This study proposed a workflow to integrate rock-mechanic tests and numerical simulations for open hole stability in chalk rocks. The focus of the model is to capture the breakout development by considering strain softening and rate dependency in the long-term behaviour. While common triaxial tests are enough to calibrate pre-failure behaviour, this study shows an open hole test is required for calibrating the post failure behaviour near the wellbore. In terms of the long time behaviour, the role of the creep deformation on wellbore stability demonstrates the possibility of breakout development near the wellbore. To the best of our knowledge, the effect of creep deformation is not commonly considered in failure criteria for the analysis and design of the safe mud-weight window and bean-up operations. Neglecting the breakout development caused by creep deformation near the wellbore can cause severe damage in uncased sections which is likely to happen in frequently and harsh shutdowns followed by rapid bean-ups.

CRediT authorship contribution statement

M.K. Medetbekova: Conceptualization, Methodology, Software, Formal analysis, Investigation, Resources, Data curation, Writing – original draft, Writing – review & editing, Visualization, Experiment, Validation. **M.R. Hajiabadi:** Formal analysis, Writing – review & editing. **A. Brovelli:** Software, Formal analysis. **H.F. Christensen:** Experiment. **H.M. Nick:** Conceptualization, Methodology, Writing – review & editing, Supervision, Project administration, Funding acquisition.

Declaration of competing interest

The authors declare that they have no known competing financial interests or personal relationships that could have appeared to influence the work reported in this paper.

Acknowledgements

We kindly thank Bertold Plischke from Isamgeo GmbH for helping, while this research was being carried out. Authors also would like to thank Geo for its contribution with regards to conventional rock mechanics and SLH testing. This project has received funding from the European Union's Horizon 2020 research and innovation programme under grant agreement No 654662 as well as the Danish Hydrocarbon Research and Technology Centre under the Advanced Water Flooding programme. The 3D Imaging Center at The Technical University of Denmark is gratefully acknowledged for providing access to X-ray tomography equipment.

Appendix A. Chalk constitutive model

The shear failure is given by the Mohr–Coulomb criterion with taking into account the effect of the intermediate principal stress:

$$F = \sqrt{J_2^C}(cos\theta + \frac{sin\varphi sin\theta}{\sqrt{3}} - \zeta(2cos2\theta - 1)) - (p' sin\varphi + ccos\varphi_{peak}) \quad (1)$$

with: J_2^C - second invariant of deviatoric stress for a Cosserat model. If no Cosserat formulation is used, J_2^C corresponds to the classical second invariant of deviatoric stress; φ - friction angle, c - cohesion; θ - Lode's angle, ζ - scales the impact of the intermediate principal stress, p' - mean effective stress.

The cohesion c and the angle of friction φ are varied in the course of hardening/softening. Hardening and softening in case of shear failure are functions of equivalent plastic strain e_{pl} incrementally determined as

$$de_{pl} = \sqrt{2((d\varepsilon_{xx}^{pl} - d\varepsilon_v^{pl})^2 + (d\varepsilon_{yy}^{pl} - d\varepsilon_v^{pl})^2 + (d\varepsilon_{zz}^{pl} - d\varepsilon_v^{pl})^2 + (d\varepsilon_{xy}^{pl})^2 + (d\varepsilon_{yz}^{pl})^2 + (d\varepsilon_{zx}^{pl})^2)} \quad (2)$$

In the case of the equivalent plastic strain being lower than the equivalent plastic strain at the peak strength e_{pl}^{peak}, the material hardens by increasing the angle of friction from an initial φ_{ini} to a peak value φ_{peak}. That reads for $e_{pl} < e_{pl}^{peak}$:

$$\varphi = \varphi_{ini} + ((\varphi_{peak} - \varphi_{ini})\sqrt{2e_{pl}e_{pl}^{peak} - e_{pl}^2})/e_{pl}^{peak} \quad (3)$$

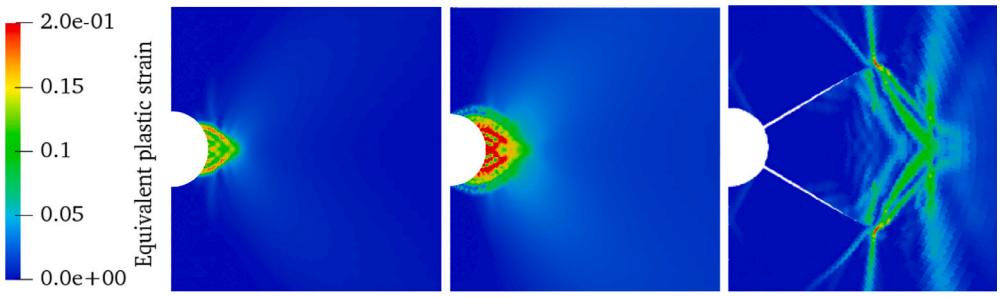

Fig. 12. Development of the equivalent plastic strain at the circular borehole wall (a) calculated after reducing the bottom hole pressure by 12 MPa and pore fluid pressure by 9 MPa at boundaries of 5 m; (b) calculated for a creep time lasting 50 days with constant bottom hole pressure of 12 MPa and pore pressure at the boundaries of 5 m with 16 MPa. And for the borehole with wing geometry: (c) development of the equivalent plastic strain at the borehole wall calculated after reducing the bottom hole pressure by 6 MPa and pore fluid pressure by 3.8 MPa at boundaries of 5 m. Wings nearly closed under simulated load conditions.

After reaching the peak strength, there is an exponential decline:

$$\varphi = (\varphi_{peak} - \varphi_{res})e^{-\chi(e_{pl}-e_{pl}^{peak})} + \varphi_{res} \tag{4}$$

Cohesion is assumed to be constant until the peak strength is reached. Cohesion c may decline either linearly or exponentially. In linear form Cohesion declines

$$c = c_0 - \eta(e_{pl} - e_{pl}^{peak}) \tag{5}$$

until the residual cohesion c_{res}. In exponential form Cohesion declines

$$c = 0.9(c_0 - c_{res})e^{-\chi(e_{pl}-2e_{pl}^{peak})} + c_{res} \tag{6}$$

which becomes effective after a slight sinus-shaped decline from c_0 to $0.9(c_0 - c_{res}) + c_{res}$ for $e_{pl}^{peak} < e_{pl} < 2e_{pl}^{peak}$. Exponential softening is preferred in the Single Element model, in order to reproduce the effects from shear strain localization.Non-associated flow rule is applied on the shear failure surface. The plastic flow rule is controlled by the plastic potential that uses the same function as the yield surface, but the friction angle φ is replaced by the dilatancy angle ψ. For the dilatancy angle ψ, the same hardening and softening rules apply as for the friction with one modification: Softening starts only after the equivalent plastic strain has reached $10e_{pl}^{peak}$:

$$\psi = (\psi_{peak} - \psi_{res})e^{-\chi(e_{pl}-10e_{pl}^{peak})} + \psi_{res} \tag{7}$$

For smaller plastic strains, but greater than e_{pl}^{peak}, the peak dilatancy applies.

The yield surface for the pore collapse is given by an elliptical cap in the $p' - q$ diagram, similar as for a Modified Cam–Clay model:

$$F = \left(\frac{2(p' + A_0)}{(p_{cc} + A_0)} - 1\right)^2 + \left(\frac{2q}{M(p_{cc} + A_0)}\right)^2 - 1 \tag{8}$$

with: q - deviatoric stress; p_{cc} - hydrostatic pore collapse strength for the current volumetric plastic strain rate; M - material parameter (similar in Modified Cam–Clay model which defines the slope of the critical state line) determines the shape of the elliptical yield surface; A_0 - parameter which denotes a shift of the ellipse along the p' axis.

The associated flow rule is applied on the pore collapse failure surface. The rate dependency of the pore collapse strength on the volumetric plastic strain rate is based on the de-Waal's model (de Waal and Smits, 1988):

$$p_{cc} = p_{c0}\left(\frac{\dot{\varepsilon}_v^{pl}}{\dot{\varepsilon}_0}\right)^b \tag{9}$$

with: $\dot{\varepsilon}_0$ denotes the reference volumetric plastic strain rate and b is a material parameter, representing the creep effect (Amour et al., 2020, 2021); p_{c0} defines the standard hydrostatic pore collapse strength at the reference rate which depends on the volumetric plastic strain and it is governed by the hardening parameter h:

$$dp_{c0} = h d\varepsilon_v^{pl} \tag{10}$$

The hardening parameter h increases as the porosity ϕ decreases due to progressing pore collapse.

$$h = h_c - h_n\phi \tag{11}$$

At the onset of pore collapse, the volumetric plastic strain rate increases, inducing an increase of p_{cc}. On the other hand, when the rate declines, p_{cc} declines and the strain hardening is required to adjust p_{cc} to the current state of stress, resulting in creep strain. It must be noted that if both shear and pore collapse criteria are violated, the preference is given to the shear failure.

Appendix B. Supplementary data

Supplementary material related to this article can be found online at https://doi.org/10.1016/j.petrol.2021.109365. Deterministic sensitivity analysis was carried out in order to investigate the sensitivity of the results to variationsin input parameters for the wellbore stability analysis derived from a 2D modelling of the SLH test.

References

Abdelghany, W.K., Radwan, A.E., Elkhawaga, M.A., Wood, D.A., Sen, S., Kassem, A.A., 2021. Geomechanical modeling using the depth-of-damage approach to achieve successful underbalanced drilling in the gulf of suez rift basin. J. Pet. Sci. Eng. 202, 108311.

Amour, F, Christensen, HF, Hajiabadi, MR, Nick, HM, 2021. Effects of porosity and water saturation on the yield surface of upper cretaceous reservoir chalks from the danish north sea. Journal of Geophysical Research: Solid Earth 126 (3), e2020JB020608.

Amour, F., Hajiabadi, M., Nick, H., 2020. Building a comprehensive geomechanical model for chalk compaction. phase 1: Model calibration from plug to reservoir scale. In: 54th US Rock Mechanics/Geomechanics Symposium. American Rock Mechanics Association.

Andersen, A., 1995. Petroleum Research in North Sea Chalk. Joint Chalk Research, Phase IV.

Andersen, M., Foged, N., Pedersen, H., 1992. The rate-type compaction of a weak north sea chalk. In: 33rd US Rock Mech. Symposium, Santa Fe, New Mexico.

Bingham, J., 1916. An investigation of the laws of plastic flow. US Bur. Stand. Bull. 13, 309–353.

Cassiani, G., Brovelli, A., Hueckel, T., 2017. A strain-rate-dependent modified cam-clay model for the simulation of soil/rock compaction. Geomech. Energy Environ. 11, 42–51. http://dx.doi.org/10.1016/j.gete.2017.07.001.

Christensen, H., Loe, N., Plischke, B., Havmøller, O., Stage, M., 2004. Impact of the Intermediate Principal Stress on Rock Strength: Polyaxial Testing and Numerical Simulations. American Rock Mechanics Association.

Cloud, K.W., 1975. The Diagenesis of the Austin Chalk (Master's thesis). University of Texas at Dallas, Texas.

Collin, F., Cui, Y.J., Schroeder, C., Charlier, R., 2002. Mechanical behaviour of Lixhe chalk partly saturated by oil and water: Experiment and modelling. Int. J. Numer. Anal. Methods Geomech. 26, 897–924. http://dx.doi.org/10.1002/nag.229.

Corbett, K., Friedman, M., Spang, J., 1987. Fracture development and mechanical stratigraphy of Austin Chalk, Texas. AAPG Bull. 71, 17–28. http://dx.doi.org/10.1306/94886D35-1704-11D7-8645000102C1865D, URL: http://www.sciencedirect.com/science/article/pii/0148906287909259.

Cui, S., Liu, H., Meng, Y., Fan, Y., Wang, J., Han, Z., 2020. Study on mechanical properties and wellbore stability of deep brittle shale. J. Pet. Sci. Eng. 194, 107500. http://dx.doi.org/10.1016/j.petrol.2020.107500, URL: https://www.sciencedirect.com/science/article/pii/S0920410520305714.

Cuss, R., Rutter, E., Holloway, R., 2003. Experimental observations of the mechanics of borehole failure in porous sandstone. Int. J. Rock Mech. Min. Sci. 40, 747–761. http://dx.doi.org/10.1016/S1365-1609(03)00068-6.

Datcheva, M., Charlier, R., Collin, F., 2001. Constitutive equations and numerical modelling of time effects in Soft Porous Rocks. In: Numerical Analysis and Its Applications. NAA 2000. In: Lecture Notes in Computer Science, pp. 222–229.

De Gennaro, V., Delage, P., Cui, Y., Schroeder, C., Collin, F., 2003. Time-dependent behaviour of oil reservoir chalk: A multiphase approach. Soils Found. 131–147.

Dravis, J., 1980. Sedimentology and Diagenesis of the Upper Cretaceous Austin Chalk Formation, South Texas and Northern Mexico (PhD diss.). Rice University, p. 70.

Dunham, R., 1962. Classification of Carbonate Rocks According to Depositional Texture. American Association of Petroleum Geologists, pp. 108–121.

Gao, C., Gray, K., 2020. Infill well wellbore stability analysis by considering plasticity, stress arching, lateral deformation and inhomogeneous depletion of the reservoir. J. Pet. Sci. Eng. 195, 107610. http://dx.doi.org/10.1016/j.petrol.2020.107610, URL: https://www.sciencedirect.com/science/article/pii/S0920410520306781.

Gutierrez, M., Hickman, R., 2011. Model for pore-fluid induced degradation of soft rocks. Springer Ser. Geomech. Geoeng. 5, 167–185. http://dx.doi.org/10.1007/978-3-642-18284-6_10.

Haimson, B, 2007. Micromechanisms of borehole instability leading to breakouts in rocks. International Journal of Rock Mechanics and Mining Sciences 44 (2), 157–173.

Hajiabadi, M.R., Medetbekova, M.K., Nick, H.M., 2020. Application of a modified strain rate dependent Constitutive Model for Well-bore stability analyses in Chalk Reservoirs. In: American Rock Mechanics Association ARMA-2020-1665. pp. 775–782.

Hajiabadi, M.R., Nick, H.M., 2020. A modified strain rate dependent constitutive model for chalk and porous rock. Int. J. Rock Mech. Min. Sci. 134, 104406. http://dx.doi.org/10.1016/j.ijrmms.2020.104406, URL: http://www.sciencedirect.com/science/article/pii/S1365160920303579.

Hamilton, J., Shafer, J., 1991. Measurement of pore compressibility characteristics in rock exhibiting 'pore collapse' and volumetric creep. In: The Society of Core Analysts Annual Technical Conference Preprints, 3 (August 21-22).

Hickman, R., 2004. Formulation and Implementation of a Constitutive Model for Soft Rock. Virginia Polytechnic Institute and State University, Department of Civil Engineering, pp. 2–4.

Hickman, R., Gutierrez, M., 2008. Formulation of a three-dimensional rate-dependent constitutive model for chalk and porous rocks. Int. J. Numer. Anal. Methods Geomech. 32, 189–213. http://dx.doi.org/10.1002/nag, arXiv:nag.2347.

Homand, S., Shao, J.F., 2000. Mechanical behaviour of a porous chalk and effect of saturating fluid. Mech. Cohesive-Frict. Mater. 5, 583–606. http://dx.doi.org/10.1002/1099-1484(200010)5:7<583::AID-CFM110>3.0.CO;2-J.

Huang, Z., Huang, Z., 2019. Review of radial jet drilling and the key issues to be applied in new geo-energy exploitation. Energy Procedia 158, 5969–5974. http://dx.doi.org/10.1016/j.egypro.2019.01.524, URL: https://www.sciencedirect.com/science/article/pii/S187661021930548X. Innovative Solutions for Energy Transitions.

ISRM, 1983. Suggested Method for Determining the Strength of Rock Materials in Triaxial Compression: Revised Version. International Society for Rock Mechanics, Lisboa, Portugal.

Kamel, A., 2017. Radial Jet Drilling: A Technical Review. SPE-183740-MS, Society of Petroleum Engineers, pp. 6–9.

Kassem, A.A., Sen, S., Radwan, A.E., Abdelghany, W.K., Abioui, M., 2021. Effect of depletion and fluid injection in the mesozoic and paleozoic sandstone reservoirs of the october oil field, central gulf of suez basin: implications on drilling, production and reservoir stability. Nat. Resour. Res. 30, 2587–2606.

Khoei, A., 2010. Computational Plasticity in Powder Forming Processes. Elsevier Science, URL: https://books.google.dk/books?id=TKEQjVGTSHcC.

Kristiansen, T., Plischke, B., 2010. History matched full field geomechanics model of the valhall field including water weakening and re-pressurisation. In: SPE EUROPEC/EAGE Annual Conference and Exhibition, 14-17 June. Barcelona, Spain. pp. 1–21. http://dx.doi.org/10.2523/131505-ms.

Li, T., Rutqvist, J., Hu, M., et al., 2021. Tough-rfpa: Coupled thermal-hydraulic-mechanical rock failure process analysis with application to deep geothermal wells. Int. J. Rock Mech. Min. Sci. 142, 104726.

Liao, H.-L., Jia, X., Niu, J.-L., Shi, Y.-C., Gu, H.-C., Xu, J.-F., 2020. Flow structure and rock-breaking feature of the self-rotating nozzle for radial jet drilling. Pet. Sci. 17, 211–221.

Lv, A., Ramandi, H.L., Masoumi, H., Saadatfar, M., Regenauer-Lieb, K., Roshan, H., 2019. Analytical and experimental investigation of pore pressure induced strain softening around boreholes. Int. J. Rock Mech. Min. Sci. 113, 1–10.

Martins, A., Santana, M., Goncalves, C., Gaspari, E., Campos, W., Perez, J., 1999. Evaluating the transport of solids generated by shale instabilities in erw drilling part ii: Case studies. In: Presented at the 1999 SPE annual Technical Conference and Exhibition, 3-6 October, Houston, Texas. SPE 56560.

McLean, M., Addis, M., 1990. Wellbore stability analysis: a review of current methods of analysis and their field application. In: IADC/SPE Drilling Conference held in Houston, Texas, Feb 27-March 2.

McLellan, P., 1996. Assessing the risk of wellbore instability in horizontal and inclined wells. J. Can. Pet. Technol. 35.

Medetbekova, M.K., Christensen, H.F., Amour, F., Salimzadeh, S., Nick, H.M., 2020b. High pressure jet drilling effect in chalk and alteration of local geomechanics properties surrounding the radial hole. Int. J. Mech. Sci. 105954.

Medetbekova, M.K., Christensen, H., Salimzadeh, S., Bakker, R., Nick, H., 2020a. Experimental investigation of drilling lateral boreholes in chalk rocks with high-pressure jets. Int. J. Geomech. 20, 04020049.

Medetbekova, M.K., Hajiabadi, M.R., Christensen, H., Brovelli, A., Shamsolhodaei, A., Sørensen, H., Müter, D., Nick, H.M., 2020c. Evaluation of the behaviour of the lateral boreholes in the Gorm chalk field. Int. J. Rock Mech. Min. Sci..

Meng, M., Baldino, S., Miska, S., Takach, N., 2019a. Wellbore stability in naturally fractured formations featuring dual-porosity/single-permeability and finite radial fluid discharge. J. Pet. Sci. Eng. 174, 790–803.

Meng, M., Zamanipour, Z., Miska, S., Yu, M., Ozbayoglu, E., 2019b. Dynamic wellbore stability analysis under tripping operations. Rock Mech. Rock Eng. 52, 3063–3083.

Monjoie, A., Schroeder, C., Pringnon, P., Yernaux, C., DaSilva, F., Debande, G., 1990. Establishment of constitutive Laws of Chalk and Long Term Tests. In: Presented at the Third North Sea Chalk Symposium.

Mowar, S., Zaman, M., Stearns, D., Roegiers, J., 1996. Micro-mechanisms of pore collapse in limestone. J. Pet. Sci. Eng. 15, 221–235. http://dx.doi.org/10.1016/0920-4105(95)00065-8.

Papamichos, E., 2010. Borehole failure analysis in a sandstone under anisotropic stresses. Int. J. Numer. Anal. Methods Geomech. 34, 581–603.

Papamichos, E., Brignoli, M., Santarelli, F., 1997. An experimental and theoretical study of a partially saturated collapsible rock. Mech. Cohesive-Frict. Mater. 251–278.

Papamichos, E., Vardoulakis, I., Tronvoll, J., Skjrstein, A., 2001. Volumetric sand production model and experiment. Int. J. Numer. Anal. Methods Geomech. 25, 789–808. http://dx.doi.org/10.1002/nag.154.

Papanastasiou, P., 2000. Localization of deformation and failure around elliptical perforations based on a polar continuum. Comput. Mech. 26, 352–361.

Papanastasiou, P.C., Vardoulakis, I.G., 1992. Numerical treatment of progressive localization in relation to borehole stability. Int. J. Numer. Anal. Methods Geomech. 16, 389–424.

Paslay, P., Cheatham, Jr., J., et al., 1963. Rock stresses induced by flow of fluids into boreholes. Soc. Pet. Eng. J. 3, 85–94.

Plischke, B., 1994. Finite element analysis of compaction and subsidence — Experience gained from several chalk fields. Soc. Pet. Eng. - Rock Mech. Pet. Eng. 1994, 795–802. http://dx.doi.org/10.2523/28129-ms.

Pruiksma, J.P., Breunese, J.N., van Thienen-Visser, K., de Waal, J.A., 2015. Isotach formulation of the rate type compaction model for sandstone. Int. J. Rock Mech. Min. Sci. 78, 127–132. http://dx.doi.org/10.1016/j.ijrmms.2015.06.002.

Radwan, A., Sen, S., 2021. Stress path analysis for characterization of in situ stress state and effect of reservoir depletion on present-day stress magnitudes: Reservoir geomechanical modeling in the gulf of suez rift basin, egypt. Nat. Resour. Res. 30, 463–478.

Reinsch, T., Paap, B., Hahn, S., Wittig, V., van den Berg, S., 2018a. Insights into the radial water jet drilling technology – Application in a quarry. J. Rock Mech. Geotech. Eng. http://dx.doi.org/10.1016/j.jrmge.2018.02.001.

Reinsch, T., Paap, B., Hahn, S., Wittig, V., van den Berg, S., 2018b. Insights into the radial water jet drilling technology – application in a quarry. J. Rock Mech. Geotech. Eng. 10, 236–248. http://dx.doi.org/10.1016/j.jrmge.2018.02.001, URL: https://www.sciencedirect.com/science/article/pii/S1674775517304651.

Risnes, R., Bratli, R.K., Horsrud, P., et al., 1982. Sand stresses around a wellbore. Soc. Pet. Eng. J. 22, 883–898.

Roscoe, K., Burland, J., 1968. On the generalised stress–strain behaviour of 'wet' clay. Eng. Plast. 15, 535–609.

Santos, R., Ferreira, F.H., 2015. Wellbore stability model for standalone liner completed wells in carbonate reservoirs subjected to Acidizing Jobs - I. Dissolution-Induced Mechanical Weakening model. In: Offshore Technology Conference. OTC Brasil, Rio de Janeiro, Brazil, http://dx.doi.org/10.4043/26290-ms.

Smits, R., de Waal, J., van Kooten, J., 1986. Prediction of abrupt reservoir compaction and subsidence due to pore collapse in carbonates. SPE preprint 15642.

Sulem, I., Vardoulakis, I., 1991. Bifurcation analysis of the triaxial test on rock specimen. a theretical model for shape and size effects. Acta Mech. 83, 195–212.

Tan, M., Yaakub, C.P., Chen, X., Willoughby, D., Choi, S., Wu, B., 2004. Wellbore sability of extended reach wells in an oil field in sarawak basin, south china sea. In: Presented at the SPE Asia Pacific Oil and Gas Conference and Exhibition, 18-20 October, Perth, Australia. SPE 88609.

Tronvoll, J., Skjaerstein, A., Papamichos, E., 1997. Sand production: mechanical failure or hydrodynamic erosion. Int. J. Rock Mech. Min. Sci. 34, 465. http://dx.doi.org/10.1016/S1365-1609(97)00195-0.

Vardoulakis, I., 2018. Cosserat Continuum Mechanics: With Applications to Granular Media. In: Lecture Notes in Applied and Computational Mechanics, Springer International Publishing, URL: https://books.google.dk/books?id=ehdnDwAAQBAJ.

Veeken, C., Walters, J., Kenter, C., Davies, D., et al., 1989. Use of plasticity models for predicting borehole stability. In: ISRM International Symposium. International Society for Rock Mechanics and Rock Engineering.

de Waal, J., 1986. On the Rate Type Compaction Behaviour of Sandstone Reservoir Rock (Ph.D.thesis). Delft University.

de Waal, J., Smits, R., 1988. Prediction of reservoir compaction and surface subsidence: Field application of a new model. SPE Form. Eval. 3, 347–356. http://dx.doi.org/10.2118/14214-pa.

Zaman, M., Abdulraheem, A., Roegiers, J., 1995. Chapter 8 Reservoir compaction and surface subsidence in the North Sea Ekofisk field. In: Subsidence Due to Fluid Withdrawal. Developments in Petroleum Science, pp. 373–423.

Zhang, L., Jiang, M., Li, W., Bian, Y., 2020. A new analytical model of wellbore collapse pressure based on stability theory. J. Pet. Sci. Eng. 188, 106928. http://dx.doi.org/10.1016/j.petrol.2020.106928, URL: https://www.sciencedirect.com/science/article/pii/S0920410520300279.

Zobak, M., 2010. Reservoir Geomechanics.